







Unveiling the spin-to-charge current conversion signal in the topological insulator Bi_2Se_3 by means of spin pumping experiments

J. B. S. Mendes ^{1,*}, M. Gamino ^{2,3}, R. O. Cunha ^{1,4}, J. E. Abrão ², S. M. Rezende ² and A. Azevedo ²

¹*Departamento de Física, Universidade Federal de Viçosa, 36570-900 Viçosa, Minas Gerais, Brazil*

²*Departamento de Física, Universidade Federal de Pernambuco, 50670-901 Recife, Pernambuco, Brazil*

³*Departamento de Física, Universidade Federal do Rio Grande do Norte, 59078-900 Natal, Rio Grande do Norte, Brazil*

⁴*Centro Interdisciplinar de Ciências da Natureza, Universidade Federal da Integração Latino-Americana, 85867-970 Foz do Iguacu, Paraná, Brazil*



(Received 9 March 2020; revised 28 August 2020; accepted 27 January 2021; published 22 February 2021)

We report an investigation of the spin-to-charge current conversion in sputter-deposited films of the topological insulator Bi_2Se_3 onto single crystalline layers of yttrium iron garnet ($\text{YIG-Y}_3\text{Fe}_5\text{O}_{12}$) and polycrystalline films of permalloy ($\text{Py-Ni}_{81}\text{Fe}_{19}$). Pure spin current was injected into the Bi_2Se_3 layer by means of the spin pumping process produced by the spin precession in microwave driven ferromagnetic resonance of the ferromagnetic film. The spin-to-charge current conversion occurring at the Bi_2Se_3 /ferromagnet interface is attributed to the inverse Rashba-Edelstein effect (IREE). From the data, we verified that the voltage generated by the spin-to-charge current conversion process in Bi_2Se_3 has the same polarity as the inverse spin Hall effect in Ta, which is opposite to the one in Pt. Also, from the dependence of the voltage on the Bi_2Se_3 thickness we were able to calculate the IREE length values and found that $1.2 \text{ nm} \leq |\lambda_{\text{IREE}}| \leq 2.2 \text{ nm}$. This result allows us to conclude that indeed the surface states of Bi_2Se_3 have a dominant role in the spin-to-charge current conversion process, and the mechanism based on the spin diffusion process plays a secondary role.

DOI: [10.1103/PhysRevMaterials.5.024206](https://doi.org/10.1103/PhysRevMaterials.5.024206)

I. INTRODUCTION

The investigation of materials with strong spin-orbit coupling (SOC) has made it possible to develop different techniques for the detection of spin currents in nonmagnetic materials and has given birth to an emergent subfield of spintronics, named spin orbitronics [1–3]. Despite being a subject of interest for many years in investigations of magnetocrystalline anisotropy, the SOC has been pivotal to the progress of spintronics in the last decade. In particular, heavy metals, such as Pt and Ta, have been used as efficient materials for mutual conversion between spin and charge currents via direct and inverse spin Hall effects (SHE and ISHE, respectively) [4–7]. Lately, there has been significant progress towards developing materials with strong SOC, which can produce current-driven torques strong enough to switch the magnetization of a ferromagnetic (FM) layer in a spin-valve structure. The improvement in SHE has been observed in a variety of systems that include SOC enhancement driven by surface roughness and volume impurities [8–11], in two-dimensional (2D) materials [12], and interfacial effects [13–15].

Indeed, many spintronics phenomena driven by interface-induced SOC have been recently investigated. For instance, the inverse Rashba-Edelstein effect (IREE) [16,17] was identified in the spin-to-charge current conversion [13] in interface systems [18–25] and in topological insulators (TIs) [26–29]. In particular, TIs are quantum materials that display electronic

properties of insulators in the bulk and conducting states at the surface that are topologically protected by time reversal symmetry. These unique properties make TIs excellent candidates for many scientific applications in spintronics, quantum computation, magnetic monopoles, highly correlated electron systems, and in optical tweezers [30–34]. Among the 3D TIs, Bi_2Se_3 is an exceptional material with large band gap of 0.35 eV and with surface spectrum consisting of a single Dirac cone roughly centered within the gap [30]. Most TIs used in spintronics studies are grown by molecular beam epitaxy (MBE) [29,35], but high quality Bi_2Se_3 samples have been grown by magnetron sputtering [23,28,36].

The spin Hall effect that dominates the conversion between spin and charge currents in 3D systems has limited use in systems with reduced dimensions. Owing to the transverse nature of the spin transport phenomena, SHE is a bulk effect occurring within a volume limited by the spin-diffusion length (λ_{sd}) [15]. However, when a 3D spin current density J_S [A/m^2] is injected through an interface with high SOC, it generates a 2D charge current density J_C [A/m] by means of the IREE. In this case, the ratio $J_C/J_S = (2e/\hbar)\lambda_{\text{IREE}}$ defines a length (λ_{IREE}) that is used as measurement of the efficiency of the spin-to-charge current conversion [2,13]. Not only the absolute value of λ_{IREE} , but also its polarity must be of interest to understand the physics behind the interplay between spin and charge currents.

Here we report an investigation of the robust spin-to-charge current conversion in bilayers of Bi_2Se_3 /YIG, ($\text{YIG-Y}_3\text{Fe}_5\text{O}_{12}$, yttrium iron garnet) by means of ferromagnetic resonance driven spin pumping (FMR-SP) at room

*Corresponding author: joaquim.mendes@ufv.br

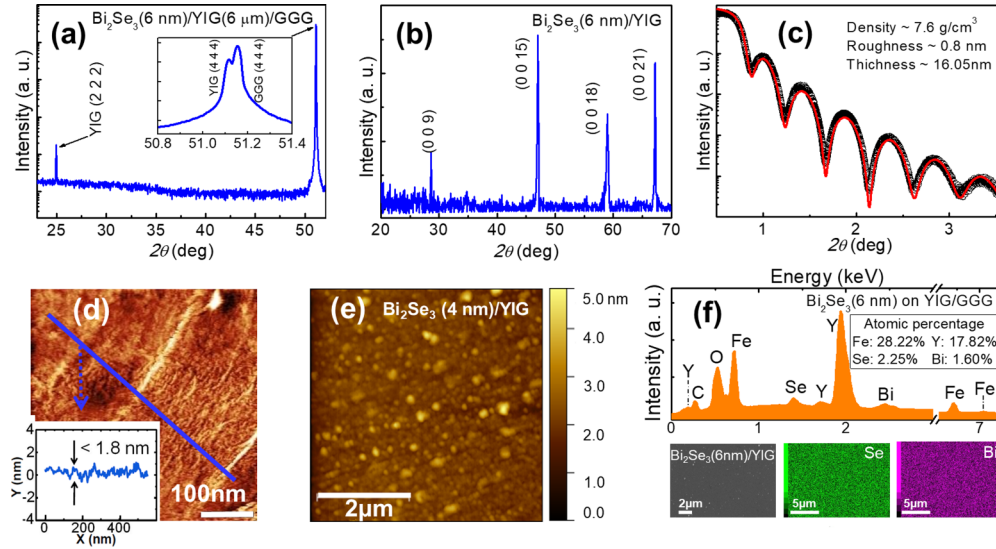


FIG. 1. (a) Out-of-plane XRD patterns (θ - 2θ scans) of Bi_2Se_3 film grown on YIG/GGG substrate. The XRD spectrum at high resolution detailing the positions of the peaks of the YIG film and the GGG substrate is shown in the inset. (b) The GIXRD pattern of the $\text{Bi}_2\text{Se}_3(6\text{ nm})/\text{YIG}/\text{GGG}$ sample. (c) XRR spectra of the Bi_2Se_3 thin film ($t \approx 16\text{ nm}$). The red solid line across the XRR data indicates the best fitting obtained for the thickness calibration. (d) AFM image of the YIG film surface. The line trace in (d) confirms that the YIG surface has a very small roughness. (e) AFM image of the surface of the $\text{Bi}_2\text{Se}_3(4\text{ nm})/\text{YIG}(6\text{ }\mu\text{m})/\text{GGG}$ sample. (f) EDX spectrum (top) from an arbitrary region in the sample of $\text{Bi}_2\text{Se}_3(6\text{ nm})/\text{YIG}$ and EDX maps (bottom) showing that the Bi and Se are evenly distributed over the entire surface of the film.

temperature. The pure spin-current density (J_S), which flows across the $\text{Bi}_2\text{Se}_3(t)/\text{YIG}$ interface due to the YIG magnetization precession, is converted into a transversal charge current density (J_C) that is detected by measuring a DC voltage between two edge contacts. The YIG films have in-plane magnetization and thus the magnetic proximity effect is expected to shift the Dirac cone sideways along the momentum direction and does not open an exchange gap (i.e., in our heterostructures, the Dirac cone of the TI film will be preserved). The $\text{Bi}_2\text{Se}_3/\text{YIG}$ interface has the advantage over the $\text{Bi}_2\text{Se}_3/\text{ferromagnetic metal}$ because it ensures cleaner interface and avoids current shunting as well as spurious spin rectification effects. Previously reported spin-to-charge current conversion experiments with sputtered $\text{Bi}_2\text{Se}_3/\text{YIG}$ were carried out in YIG grown by sputtering or MBE and, to the author's knowledge, there is no investigation about the polarity of λ_{IREE} [23,28,35]. It is important to mention that recent theoretical studies have shown that in-plane magnetic field, which breaks the time reversal symmetry, can induce the Dirac cone opening as well the existence of quantum anomalous Hall effect in TIs [37,38].

II. SAMPLE PREPARATION AND CHARACTERIZATION

The Bi_2Se_3 films with different thicknesses ($t = 4, 6,$ and 8 nm) were grown by room temperature DC sputtering onto $6\text{-}\mu\text{m}$ -thick single-crystal YIG films grown by liquid phase epitaxy (LPE) on (111) GGG ($\text{Gd}_3\text{Ga}_5\text{O}_{12}$) substrates, cut from the same wafer, having width 1.5 mm and length 3.0 mm . Prior to the deposition, the sputtering chamber is evacuated to base pressure of around 2.0×10^{-7} torr, then the Bi_2Se_3 film is DC sputtered directly from a stoichiometric target. The growth rate of films was previously established by measuring

step heights with AFM, of several layers fabricated at different deposition times using the same sputtering conditions. Figure 1(a) shows the out-of-plane x-ray diffraction (XRD) θ - 2θ scan pattern of the $\text{Bi}_2\text{Se}_3(6\text{ nm})/\text{YIG}(6\text{ }\mu\text{m})/\text{GGG}$ sample, exhibiting reflections associated with the (222) and (444) crystal planes of YIG, demonstrating the crystalline nature of the YIG film. The XRD spectrum in the inset shows the double peak corresponding to the (444) Bragg reflections of the GGG substrate and the (444) plane of YIG. In order to optimize the scattering contribution from the Bi_2Se_3 films, we used grazing incidence x-ray diffraction (GIXRD) for investigating the $\text{Bi}_2\text{Se}_3/\text{YIG}(6\text{ }\mu\text{m})/\text{GGG}$ samples. The GIXRD pattern of Fig. 1(b) clearly show the diffraction peaks characteristic of a polycrystalline Bi_2Se_3 film with preferential texture oriented along the planes: (0 0 9), (0 0 15), (0 0 18), (0 0 21), as previously reported [39,40]. The observation of (0 0 n) reflections in the GIXRD pattern implies that a significant amount of Bi_2Se_3 c -axis film orientation is in plane, and this texture is different than the usually studied samples grown by the MBE technique. We also used x-ray reflectivity (XRR) for film thickness calibration, shown in Fig. 1(c) by the well-defined Kiessig fringes for a 16-nm-thick Bi_2Se_3 film grown on Si. Figure 1(d) shows an atomic force microscopy (AFM) image of the YIG film surface and the line trace in Fig. 1(d) confirms the uniformity of the YIG film surface with very small roughness ($\sim 0.2\text{ nm}$).

On the other hand, Fig. 1(e) shows the AFM image of the sputtered granular bismuth selenide thin film ($t = 4\text{ nm}$) grown onto YIG/GGG substrate. The image shows that Bi_2Se_3 film grown onto YIG favors the formation of a granular film, with grain sizes up to $\sim 0.3\text{ }\mu\text{m}$, and has a root-mean-square (rms) surface roughness of about 1.0 nm . The typical energy-dispersive x-ray (EDX) spectrum of Bi_2Se_3 on the YIG film

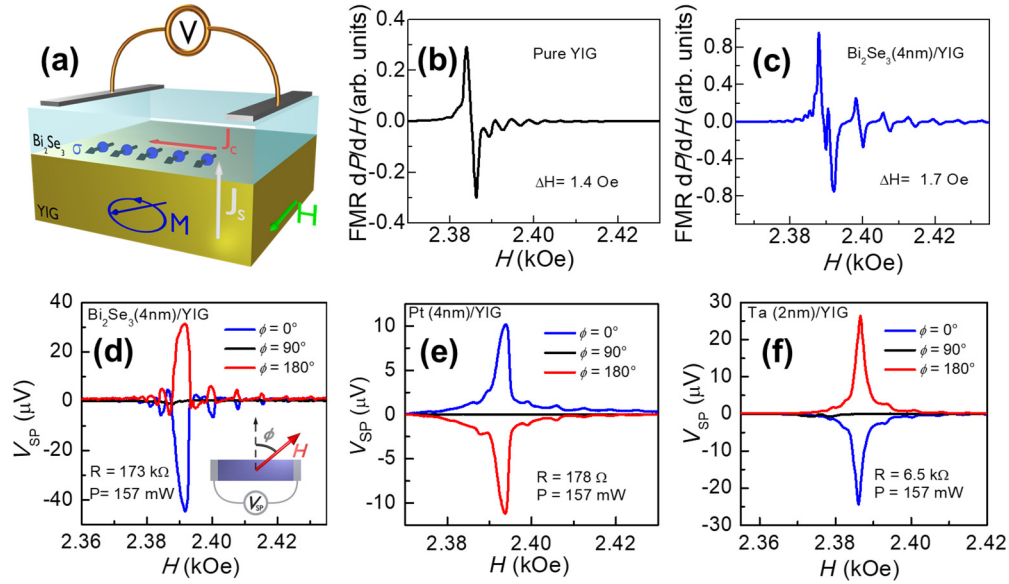


FIG. 2. (a) Schematic illustration for measurement of the FMR-SP for the spin-to-charge current conversion process at the interface. (b),(c) Field scan FMR signal for a bare YIG film with thickness of $6 \mu\text{m}$ and the bilayer of $\text{Bi}_2\text{Se}_3(4 \text{ nm})/\text{YIG}(6 \mu\text{m})$, respectively. (d) Field scan of the spin pumping voltage measured in $\text{Bi}_2\text{Se}_3(4 \text{ nm})/\text{YIG}(6 \mu\text{m})$ at three different in-plane angles as illustrated in the inset, with an incident microwave power of 157 mW . Field scans of V_{SP} for the bilayers of $\text{Pt}(4 \text{ nm})/\text{YIG}$ in (e) and $\text{Ta}(2 \text{ nm})/\text{YIG}$ in (f), obtained with the same experimental configuration used to measure V_{SP} in $\text{Bi}_2\text{Se}_3/\text{YIG}$. By comparing with Fig. 2(d) we concluded that the V_{SP} polarization of Bi_2Se_3 is the same as in Ta.

can be seen in Fig. 1(f). The EDX spectrum taken from an arbitrary region of the sample shows the presence only of yttrium (Y), iron (Fe), and oxygen (O) of the YIG film, and bismuth (Bi) and selenium (Se) of Bi_2Se_3 . The additional peak of the carbon (C) in the EDX spectrum is due to the presence of carbon tape used as support on which the samples are prepared for analysis. In the figure there are also the EDX maps showing that the Bi and Se are evenly distributed over the entire surface of the film. Different regions of the samples were analyzed, in order to confirm the results of the EDX measurements. For the different regions, the atomic percentage of Se is always larger than that of Bi. We can also see that the percentage is 2.25% for Se while that of Bi is 1.60% and the stoichiometry measured is very close to the expected nominal value.

III. SPIN-PUMPING EXPERIMENTS

For the FMR and spin-pumping experiments, the sample is mounted on the tip of a PVC rod and inserted through a hole at the bottom wall of a shorted X-band waveguide, in a position of maximum rf magnetic field and zero electric field. The loaded waveguide is placed between the poles of an electromagnet that applies a DC magnetic field \vec{H}_0 perpendicular to the in-plane rf magnetic field \vec{h}_{rf} . The spin pumping voltage (V_{SP}) is measured by means of two copper wires attached at the edges of the sample with silver paint to the electrodes and connected directly to a nanovoltmeter. Figure 2(a) shows schematically the sample setup used in the experiment of FMR-SP with electrodes at the edges. As the DC and rf magnetic fields are perpendicular to each other, the sample rod, attached to a goniometer, can be rotated so that we can investigate the angular dependence of both the

ferromagnetic resonance (FMR) signal and V_{SP} . Field scan of the derivative of the absorption power (dP/dH), at a fixed frequency of 9.5 GHz , is obtained by modulating the field \vec{H}_0 with a small sinusoidal field at 1.2 kHz and detected by a lock-in amplifier. Figure 2(b) shows the FMR spectrum of a bare YIG sample obtained with the in-plane field applied normal to the larger length with an incident power of 54 mW . The strongest line corresponds to the uniform FMR mode ($k_0 \cong 0$) with frequency given by Kittel's equation $\omega_0 = \gamma \sqrt{(H_0 + H_A)(H_0 + H_A + 4\pi M_{\text{eff}})}$, where $\gamma = 2\pi \times 2.8 \text{ GHz/kOe}$ and $4\pi M_{\text{eff}} = 4\pi M + H_s \cong 1760 \text{ G}$ for YIG. While the lines to the left of the uniform mode correspond to hybridized standing spin-wave surface modes, the lines to the right correspond to the backward volume magnetostatic modes with quantized wave number k , subjected to the appropriated boundary conditions. All modes have similar half width at half maximum linewidth (HWHM) of $\Delta H_{\text{YIG}} = 1.4 \text{ Oe}$. As shown in Fig. 2(c), the deposition of a 4.0-nm -thick film of Bi_2Se_3 on the YIG layer increases the FMR linewidth to $\Delta H_{\text{Bi}_2\text{Se}_3/\text{YIG}} = 1.7 \text{ Oe}$ mostly due to the spin pumping [41,42]. The YIG magnetization precession injects a pure spin current density \vec{J}_s , that flows perpendicularly to the $\text{Bi}_2\text{Se}_3/\text{YIG}$ interface with transverse spin polarization $\hat{\sigma}$, and is given by

$$\vec{J}_s = (\hbar g_{\text{eff}}^{\uparrow\downarrow} / 4\pi M_s^2) [\vec{M}(t) \times \partial \vec{M}(t) / \partial t], \quad (1)$$

where M_s and $M(t)$ are the saturation and time dependent magnetizations, respectively, and $g_{\text{eff}}^{\uparrow\downarrow}$ is the real part of the interfacial spin-mixing conductance, that takes into account the forward and backward flows of the spin current [41]. It is important to mention that J_s in Eq. (1) has units of energy/area. The pure spin-current density

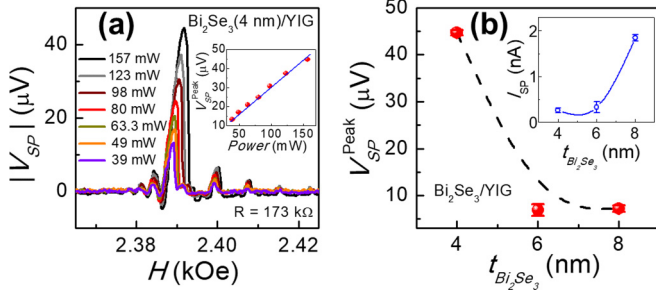


FIG. 3. (a) Field scans of $|V_{SP}|$ for several values of the incident microwave power. The inset shows the peak voltage value as function of the rf excitation power measured on the $\text{Bi}_2\text{Se}_3(4 \text{ nm})/\text{YIG}$ sample. (b) Peak voltage value measured as a function of the Bi_2Se_3 thickness for an incident power of 157 mW. The inset shows the dependence of the spin pumping current ($I_{SP} = V_{SP}^{\text{peak}}/R$).

\vec{J}_S is converted into a transverse charge current density (J_C) that is detected by the measured voltage V_{SP} and $g_{\text{eff}}^{\uparrow\downarrow}$ of the $\text{Bi}_2\text{Se}_3/\text{YIG}$ interface can be estimated by the additional FMR linewidth broadening, i.e., $g_{\text{eff}}^{\uparrow\downarrow} = (4\pi M t_{\text{FM}}/\hbar\omega)(\Delta H_{\text{Bi}_2\text{Se}_3/\text{YIG}} - \Delta H_{\text{YIG}})$, where $\omega = 2\pi f$ and t_{FM} is the ferromagnetic (FM) layer thickness for thin FM films (or the coherence length for films such as the one used here). Considering that for the Pt/YIG bilayer obtained with the same YIG, $\Delta H_{\text{Pt}/\text{YIG}} - \Delta H_{\text{YIG}} = 0.55 \text{ Oe}$ and $g_{\text{eff}}^{\uparrow\downarrow}(\text{Pt}/\text{YIG}) = 10^{14} \text{ cm}^{-2}$, we obtain $g_{\text{eff}}^{\uparrow\downarrow}(\text{Bi}_2\text{Se}_3/\text{YIG}) \approx 5.4 \times 10^{13} \text{ cm}^{-2}$.

Figure 2(d) shows the spin pumping voltage V_{SP} obtained by sweeping the DC field with no AC field modulation, measured in a bilayer of $\text{Bi}_2\text{Se}_3(4 \text{ nm})/\text{YIG}$ for three in-plane field directions given by $\phi = 0^\circ$, 90° , and 180° , as illustrated in the inset. As expected from the equation $\vec{J}_C = \theta_{\text{SH}}(2e/\hbar)(\vec{J}_S \times \hat{\sigma})$, where $\hat{\sigma} \parallel \vec{H}$, the charge current flows in plane so that the value of V_{SP} is maximum for $\phi = 0^\circ$ and $\phi = 180^\circ$ for blue and red curves, respectively, and is null for $\phi = 90^\circ$, as shown by the black curve. The asymmetry between the positive and negative peaks is similar to that observed in other bilayer systems and it is attributed to thermoelectric effects [43]. For comparison, the field scan spectra of V_{SP} for the bilayers Pt(4 nm)/YIG and Ta(2 nm)/YIG obtained with the same experimental configuration are shown in Figs. 2(e) and 2(f), respectively. By comparing with Fig. 2(d) we concluded that the V_{SP} polarization of Bi_2Se_3 is the same as the one for Ta, and opposite to the one for Pt.

Figure 3(a) shows $|V_{SP}|$ field scans for the field at $\phi = 0^\circ$ measured with several rf powers. The linear dependence, shown in the inset of Fig. 3(a), confirms that the FMR measurements were carried out in the linear regime of excitation. Figure 3(b) shows the dependence of the peak voltage on the Bi_2Se_3 layer thickness ($t_{\text{Bi}_2\text{Se}_3}$) measured with 157 mW. Clearly, the voltage decreases with increasing $t_{\text{Bi}_2\text{Se}_3}$, in contrast with results in materials in which the spin-to-charge current conversion occurs in the bulk by ISHE, as in Pt. The decrease in the peak voltage with thickness was also observed in crystalline Bi_2Se_3 grown by MBE [35]. Despite this, one could try to explain the origin of the voltage in $\text{Bi}_2\text{Se}_3/\text{YIG}$ as due to the ISHE mechanism, where the spin pumping voltage

is given by [44–46]

$$V_{SP}(H) = \frac{R_N e \theta_{\text{SH}} \lambda_N w p_{xz} \omega g_{\text{eff}}^{\uparrow\downarrow}}{8\pi} \tanh\left(\frac{t_N}{2\lambda_N}\right) \left(\frac{h_{\text{rf}}}{\Delta H}\right)^2 \times L(H - H_R) \cos \phi. \quad (2)$$

Here, R_N , t_N , λ_N , and w are respectively the resistance, thickness, spin diffusion length, and width of the Bi_2Se_3 layer, $\omega = 2\pi f$ is the microwave frequency, and p_{xz} is a factor that expresses the ellipticity and the spatial variation of the rf magnetization of the FMR mode. Also, h_{rf} and ΔH are the applied microwave field and FMR linewidth, and $L(H - H_R)$ represents the Lorentzian function. By assuming that $2\lambda_N \gg t_N$, $\tanh(t_N/2\lambda_N) \approx t_N/2\lambda_N$, and Eq. (2) can be written as $V_{SP} = (R_N f e \theta_{\text{SH}} w p_{xz} g_{\text{eff}}^{\uparrow\downarrow} t_N/8)(h_{\text{rf}}/\Delta H)^2$. This expression does not depend on λ_N , as expected for TIs, so that t_N can be interpreted as an effective thickness attributed to the Bi_2Se_3 . From the measured quantities for the bilayer $\text{Bi}_2\text{Se}_3(4 \text{ nm})/\text{YIG}$, $R_N = 173 \text{ k}\Omega$, $g_{\text{eff}}^{\uparrow\downarrow} \approx 5.4 \times 10^{13} \text{ cm}^{-2}$, $h_{\text{rf}} = 0.055 \text{ Oe}$, $\Delta H = 1.7 \text{ Oe}$, $V_{SP} = 44.7 \mu\text{V}$, and $\theta_{\text{SH}} \approx 0.11$ (as reported in Ref. [27] for average value of θ_{SH}), the effective thickness of the Bi_2Se_3 layer is $t_N = 0.46 \text{ \AA}$. This small value is certainly unphysical for an effective layer that converts a 3D spin current density in a 3D charge current, as in the ISHE.

IV. DISCUSSION

The results in the previous section provide clear evidence that the mechanism for spin-to-charge current conversion in Bi_2Se_3 does not originate in the ISHE. As in other 2D systems, we consider that the conversion mechanism in $\text{Bi}_2\text{Se}_3/\text{YIG}$ is dominated by the IREE of surface states. Hence, we calculate the effective length $\lambda_{\text{IREE}} = (\hbar/2e)J_C/J_S$, where $V_{\text{IREE}} = R_{\text{Bi}_2\text{Se}_3} w J_C$ and $J_S = (e\omega p_{xz} g_{\text{eff}}^{\uparrow\downarrow}/16\pi)(h_{\text{rf}}/\Delta H)^2 L(H - H_R)$, with $p_{11} = 0.31$. Therefore, λ_{IREE} is given by

$$\lambda_{\text{IREE}} = \frac{4V_{\text{IREE}}}{R_{\text{Bi}_2\text{Se}_3} e w f g_{\text{eff}}^{\uparrow\downarrow} p_{xz} (h_{\text{rf}}/\Delta H)^2}. \quad (3)$$

Using the physical quantities for the bilayer $\text{Bi}_2\text{Se}_3(4 \text{ nm})/\text{YIG}$, we obtain $|\lambda_{\text{IREE}}|(t_{\text{Bi}_2\text{Se}_3} = 4 \text{ nm}) = (2.2 \pm 0.4) \times 10^{-12} \text{ m}$. For the other two bilayers we obtain $|\lambda_{\text{IREE}}|(t_{\text{Bi}_2\text{Se}_3} = 6 \text{ nm}) = (2.0 \pm 0.5) \times 10^{-12} \text{ m}$, and $|\lambda_{\text{IREE}}|(t_{\text{Bi}_2\text{Se}_3} = 8 \text{ nm}) = (1.2 \pm 0.1) \times 10^{-12} \text{ m}$. Note that the only parameters varying from sample to sample are resistance (R), average peak voltage ($\langle V_{SP} \rangle$), and the FMR linewidth $\Delta H_{\text{Bi}_2\text{Se}_3/\text{YIG}}$. The error bars in Fig. 3(b) were incorporated in λ_{IREE} by taking into account the variation of V_{SP} measured at $\phi = 0^\circ$ and 180° . Therefore, we found values that vary in the range of $1.2 \text{ pm} \leq |\lambda_{\text{IREE}}| \leq 2.2 \text{ pm}$, consistent with $0.001 \text{ nm} < \lambda_{\text{IREE}} \leq 0.11 \text{ nm}$ reported in the literature [23,35]. Although we cannot rule out the spin diffusion mechanism, the values of λ_{IREE} strongly support the role played by the surface states in the spin-to-charge current conversion process occurring in sputtered Bi_2Se_3 layers. Indeed, granular Bi_2Se_3 films grown by sputtering keep the topological insulator properties even in the nanometer scale regime. The basic mechanisms explaining the existence of topological surface states in granular films of Bi_2Se_3 is based on the electron tunneling between grain surfaces. Also, the

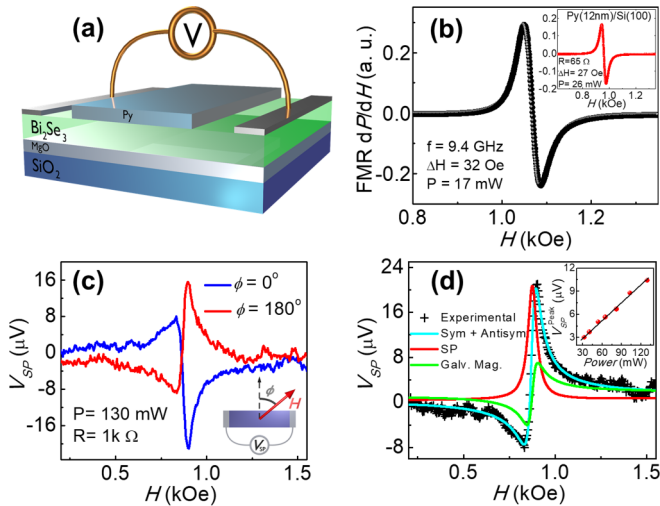


FIG. 4. (a) Sketch of the bilayer sample Py/Bi₂Se₃. In order to minimize shunting effects, the Py film partially covers the Bi₂Se₃ film surface. (b) FMR field scan for the bilayer Py(12 nm)/Bi₂Se₃(4 nm) obtained by inserting the sample in a microwave rectangular cavity. The inset shows field scan of the FMR absorption derivative (dP/dH) for a bare Py(12 nm) film. (c) Field scan of V_{SP} for two in-plane angles, measured at the same experimental configuration. (d) Decomposition of the symmetric and antisymmetric components of V_{SP} obtained by fitting the data of (c). The inset shows the dependence of the peak value of the symmetric component as a function of the microwave power, measured at $\phi = 180^\circ$.

electron quantum confinement in nanometer sized grains has been considered as the reason of the high spin-to-charge conversion effect in granular TIs [36].

To further study the polarization of the spin-to-charge current conversion process in Bi₂Se₃, we investigated the spin pumping voltage in the bilayer of Bi₂Se₃(4 nm)/Py(12 nm), where Py is permalloy (Ni₈₁Fe₁₉). The investigated sample is illustrated in Fig. 4(a), where the Py layer partially covers the Bi₂Se₃ surface, so that the electrodes are attached out of the Py layer. The sample was sputter grown onto SiO₂(300 nm)/Si(001) where a passivation layer of MgO(2 nm) was grown underneath the Bi₂Se₃ layer. Figure 4(b) shows the FMR spectrum of the bilayer Py(12 nm)/Bi₂Se₃(4 nm) in which the sample is placed in a microwave cavity resonating at 9.4 GHz with $Q \approx 2000$. Due to the spin pumping effect, the FMR linewidth (HWHM) increased to 32 Oe in comparison with the linewidth of 27 Oe of a bare Py(12 nm) layer, shown in the inset of Fig. 4(b). Figure 4(c) shows the field scan of V_{SP} measured for $\phi = 0^\circ$ and $\phi = 180^\circ$. The V_{SP} line shape is described

by the sum of symmetric and antisymmetric components, $V_{SP}(H) = V_s(H - H_R) + V_{AS}(H - H_R)$, where $V_s(H - H_R)$ is the (symmetric) Lorentzian function and $V_{AS}(H - H_R)$ is the (antisymmetric) Lorentzian derivative centered at the FMR resonance field (H_R) [46,47]. Figure 4(d) shows the corresponding symmetric (red) and antisymmetric (green) components of the V_{SP} line shape for $\phi = 180^\circ$, obtained by fitting the data (black symbols) with a sum of a Lorentzian function and Lorentzian derivative (given by the cyan curve). The inset of Fig. 4(d) shows the linear dependence of the peak value of the symmetric component as a function of the incident power. The symmetric component of V_{SP} in Bi₂Se₃/Py, which is attributed to the spin-to-charge current conversion process, has the same polarity as the one observed for V_{SP} measured in Bi₂Se₃/YIG and Ta/YIG bilayers. It is worth mentioning that as the Py layer does not fully cover the Bi₂Se₃ layer, the out of plane stray magnetic field at the edges can be significantly strong to induce a gap opening at the TI Dirac points. This effect can be detected by electron transport measurements [2].

In summary, we report an investigation of the spin-to-charge current conversion process in bilayers of Bi₂Se₃/YIG and Bi₂Se₃/Py, where the Bi₂Se₃ layer was grown by sputtering. The results obtained by means of the ferromagnetic resonance driven spin pumping technique has shed light on some aspects. The experiments reveal that the spin-to-charge current mechanism in topological insulator Bi₂Se₃ has the same polarity as the SHE in Ta, and opposite to the one in Pt. By interpreting the spin pumping voltage as due to the inverse Rashba-Edelstein effect, we calculated the value of λ_{IREE} as a function of Bi₂Se₃ thickness and the values obtained demonstrate that the surface states have a dominant role in the spin-charge conversion process. The combination of the magnetic properties of YIG and Py with strong spin-orbit coupling and dissipationless surface states topologically protected of Bi₂Se₃ might lead to spintronic devices with fast and efficient spin-charge conversion.

ACKNOWLEDGMENTS

This research was supported by Conselho Nacional de Desenvolvimento Científico e Tecnológico (CNPq), Coordenação de Aperfeiçoamento de Pessoal de Nível Superior (CAPES), Financiadora de Estudos e Projetos (FINEP), Fundação de Amparo à Ciência e Tecnologia do Estado de Pernambuco (FACEPE), Fundação Arthur Bernardes (Funarbe), Fundação de Amparo à Pesquisa do Estado de Minas Gerais (FAPEMIG) - Rede de Pesquisa em Materiais 2D and Rede de Nanomagnetismo.

[1] A. Manchon and A. Belabbes, *Solid State Phys.* **68**, 1 (2017).
 [2] A. Soumyanarayanan, N. Reyren, A. Fert, and C. Panagopoulos, *Nature (London)* **539**, 509 (2016).
 [3] A. Hoffmann and S. D. Bader, *Phys. Rev. Appl.* **4**, 047001 (2015).
 [4] M. I. Dyakonov and V. I. Perel, *Phys. Lett. A* **35**, 459 (1971).
 [5] J. E. Hirsch, *Phys. Rev. Lett.* **83**, 1834 (1999).

[6] A. Azevedo, L. H. Vilela Leão, R. L. Rodriguez-Suarez, A. B. Oliveira, and S. M. Rezende, *J. Appl. Phys.* **97**, 10C715 (2005).
 [7] E. Saitoh, M. Ueda, H. Miyajima, and G. Tatara, *Appl. Phys. Lett.* **88**, 182509 (2006).
 [8] L. Zhou, V. L. Grigoryan, S. Maekawa, X. Wang, and J. Xiao, *Phys. Rev. B* **91**, 045407 (2015).

- [9] O. Alves-Santos, E. F. Silva, M. Gamino, R. O. Cunha, J. B. S. Mendes, R. L. Rodríguez-Suárez, S. M. Rezende, and A. Azevedo, *Phys. Rev. B* **96**, 060408(R) (2017).
- [10] Y. Niimi, Y. Kawanishi, D. H. Wei, C. Deranlot, H. X. Yang, M. Chshiev, T. Valet, A. Fert, and Y. Otani, *Phys. Rev. Lett.* **109**, 156602 (2012).
- [11] Y. Niimi and Y. Otani, *Rep. Prog. Phys.* **78**, 124501 (2015).
- [12] J. Sławińska, F. T. Cerasoli, H. Wang, S. Postorino, A. Supka, S. Curtarolo, M. Fornari, and M. B. Nardelli, *2D Mater.* **6**, 025012 (2019).
- [13] O. J. C. Rojas Sánchez, L. Vila, G. Desfonds, S. Gambarelli, J. P. Attané, J. M. De Teresa, C. Magén, and A. Fert, *Nat. Commun.* **4**, 2944 (2013).
- [14] Kyoung-Whan Kim, Kyung-Jin Lee, Jairo Sinova, Hyun-Woo Lee, and M. D. Stiles, *Phys. Rev. B* **96**, 104438 (2017).
- [15] J. Sklenar, W. Zhang, M. B. Jungfleisch, W. Jiang, H. Saglam, J. E. Pearson, J. B. Ketterson, and A. Hoffmann, *J. Appl. Phys.* **120**, 180901 (2016).
- [16] Yu. A. Bychkov and É. I. Rashba, *JETP Lett.* **39**, 78 (1984).
- [17] V. M. Edelstein, *Solid State Commun.* **73**, 233 (1990).
- [18] J. B. S. Mendes, O. Alves Santos, L. M. Meireles, R. G. Lacerda, L. H. Vilela-Leão, F. L. A. Machado, R. L. Rodríguez-Suárez, A. Azevedo, and S. M. Rezende, *Phys. Rev. Lett.* **115**, 226601 (2015).
- [19] A. Nomura, T. Tashiro, H. Nakayama, and K. Ando, *Appl. Phys. Lett.* **106**, 212403 (2015).
- [20] E. Lesne, Yu Fu, S. Oyarzun, J.-C. Rojas-Sánchez, D. C. Vaz, H. Naganuma, G. Sicoli, J.-P. Attané, M. Jamet, E. Jacquet, J.-M. George, A. Barthélémy, H. Jaffrés, A. Fert, M. Bibes, and L. Vila, *Nat. Mater.* **15**, 1261 (2016).
- [21] S. Karube, K. Kondou, and Y. Otani, *Appl. Phys. Express* **9**, 033001 (2016).
- [22] M. Matsushima, Y. Ando, S. Dushenko, R. Ohshima, R. Kumamoto, T. Shinjo, and M. Shiraishi, *Appl. Phys. Lett.* **110**, 072404 (2017).
- [23] Mahendra DC, T. Liu, J.-Y. Chen, T. Peterson, P. Sahu, H. Li, Z. Zhao, M. Wu, and J. -P. Wang, *Appl. Phys. Lett.* **114**, 102401 (2019).
- [24] J. B. S. Mendes, A. Aparecido-Ferreira, J. Holanda, A. Azevedo, and S. M. Rezende, *Appl. Phys. Lett.* **112**, 242407 (2018).
- [25] J. B. S. Mendes *et al.*, *Phys. Rev. B* **99**, 214446 (2019).
- [26] A. R. Mellnik, J. S. Lee, A. Richardella, J. L. Grab, P. J. Mintun, M. H. Fischer, A. Vaezi, A. Manchon, E.-A. Kim, N. Samarth, and D. C. Ralph, *Nature (London)* **511**, 449 (2014).
- [27] M. Jamali, J.S. Lee, J.S. Jeong, F. Mahfouzi, Y. Lv, Z. Zhao, B. K. Nikolic, K. A. Mkhoyan, N. Samarth, and J. P. Wang, *Nano Lett.* **15**, 7126 (2015).
- [28] Mahendra DC, Jun-Yang Chen, Thomas Peterson, Protuysh Sahu, Bin Ma, Naser Mousavi, Ramesh Harjani, and Jian-Ping Wang, *Nano Lett.* **19**, 4836 (2019).
- [29] J. B. S. Mendes, O. Alves Santos, J. Holanda, R. P. Loreto, C. I. L. de Araujo, C.-Z. Chang, J. S. Moodera, A. Azevedo, and S. M. Rezende, *Phys. Rev. B* **96**, 180415(R) (2017).
- [30] M. Z. Hasan and C. L. Kane, *Rev. Mod. Phys.* **82**, 3045 (2010).
- [31] C. Nayak, S. H. Simon, A. Stern, M. Freedman, and S. Das Sarma, *Rev. Mod. Phys.* **80**, 1083 (2008).
- [32] X.-L. Qi, R. Li, J. Zang, and S.-C. Zhang, *Science* **323**, 1184 (2009).
- [33] L. Fu and C. L. Kane, *Phys. Rev. Lett.* **100**, 096407 (2008).
- [34] W. H. Campos, J. M. Fonseca, V. E. de Carvalho, J. B. S. Mendes, M. S. Rocha, and W. A. Moura-Melo, *ACS Photonics* **5**, 741 (2018).
- [35] H. Wang, J. Kally, J. S. Lee, T. Liu, H. Chang, D. R. Hickey, K. A. Mkhoyan, M. Wu, A. Richardella, and N. Samarth, *Phys. Rev. Lett.* **117**, 076601 (2016).
- [36] Mahendra DC *et al.*, *Nat. Mater.* **17**, 800 (2018).
- [37] X. Liu, H.-C. Hsu, and C.-X. Liu, *Phys. Rev. Lett.* **111**, 086802 (2013).
- [38] J. Zhang, Z. Liu, and J. Wang, *Phys. Rev. B* **100**, 165117 (2019).
- [39] Y. F. Lee, R. Kumar, F. Hunte, J. Narayan, and J. Schwartz, *J. Appl. Phys.* **118**, 125309 (2015).
- [40] A. Banerjee, O. Deb, K. Majhi, R. Ganesan, D. Sen, and P. S. Anil Kumar, *Nanoscale* **9**, 6755 (2017).
- [41] Y. Tserkovnyak, A. Brataas, G. E. W. Bauer, and B. I. Halperin, *Rev. Mod. Phys.* **77**, 1375 (2005).
- [42] S. M. Rezende, R. L. Rodríguez-Suárez, and A. Azevedo, *Phys. Rev. B* **88**, 014404 (2013).
- [43] H. Emoto, Y. Ando, G. Eguchi, R. Ohshima, E. Shikoh, Y. Fuseya, T. Shinjo, and M. Shiraishi, *Phys. Rev. B* **93**, 174428 (2016).
- [44] A. Hoffmann, *IEEE Trans. Magn.* **49**, 5172 (2013).
- [45] O. Mosendz, V. Vlaminck, J. E. Pearson, F. Y. Fradin, G. E. W. Bauer, S. D. Bader, and A. Hoffmann, *Phys. Rev. B* **82**, 214403 (2010).
- [46] A. Azevedo, L. H. Vilela-Leão, R. L. Rodríguez-Suárez, A. F. Lacerda Santos, and S. M. Rezende, *Phys. Rev. B* **83**, 144402 (2011).
- [47] J. B. S. Mendes, S. L. A. Mello, O. Alves Santos, R. O. Cunha, R. L. Rodríguez-Suárez, A. Azevedo, and S. M. Rezende, *Phys. Rev. B* **95**, 214405 (2017).